

Impact of vacancies on twisted bilayer graphene quantum point contactsPablo Moles ,* Francisco Domínguez-Adame , and Leonor Chico *GISC, Departamento de Física de Materiales, Universidad Complutense, E-28040 Madrid, Spain*

(Received 13 July 2023; revised 18 December 2023; accepted 21 December 2023; published 12 January 2024)

We carry out an extensive numerical study of low-temperature electronic transport in quantum point contacts based on twisted bilayer graphene. Assuming ballistic electron dynamics, quantized plateaus in the conductance are observed in defect-free samples when the twisting angle is large enough. However, plateaus are smeared out and hardly noticeable on decreasing the angle. Close to the magic angle, the conductance around the charge neutrality point drops significantly and the quantization steps visible at higher angles are no longer appreciable. Furthermore, we consider the effects of a random distribution of vacancies on the quantum point contact. Whereas the electron-hole symmetry is broken in pristine samples, we find that this symmetry is restored upon increasing the concentration of vacancies. We explain this effect by a reduction of the effective interlayer coupling due to the presence of the vacancies.

DOI: [10.1103/PhysRevB.109.045415](https://doi.org/10.1103/PhysRevB.109.045415)**I. INTRODUCTION**

Quantum point contacts (QPC), short narrow conductors between two electron reservoirs that can be electrostatically defined or etched in two-dimensional materials, are the center of attention for their prospective applications in spin, valley, and charge nanodevices [1]. The goal is to control, by varying an external perturbation (typically an electrical potential), a degree of freedom of the system. Charge noise limits the coherence times compared to spin, so graphene spintronics has been an important area of research with the aim of achieving device applications [2]. However, spin is hard to manipulate, so other degrees of freedom available in graphene-based devices, such as the valley index, are also the subject of current interest [3].

In monolayer graphene, QPCs are created by etching since a gate voltage does not open a gap in this material [4]. However, etching generally produces defects which hinder the properties of the pristine material. In contradistinction, it is possible to open a gap in bilayer graphene with Bernal stacking by applying an electric field, so a great amount of effort has been devoted to elucidate and tune its transport properties via gate voltages. Furthermore, the fabrication of electrostatic QPCs in bilayer graphene has allowed to produce one-dimensional conducting channels and probe their transport behavior [5,6]. QPC defined by electrostatic gating present fewer defects and has been shown to hold valley transport, the properties of which are still being understood [1,3,7].

Despite the aforementioned occurrence of defects and roughness in lithographically defined graphene QPCs, much effort has been devoted to improve these methods, and recently, graphene nanoconstrictions with high-quality edges have been fabricated employing a cryo-etching technique [8,9]. Due to the low edge roughness and minimal defects,

quantization of electron transport was experimentally observed, demonstrating the fabrication of low-defect QPCs via etching processes. This is especially important for twisted bilayer graphene (TBG) QPCs, in which the interplay of moiré and edge localization should be studied in systems with well-defined edges [10–13]. In moiré systems, the interlayer coupling is inhomogeneous, being stronger in regions with direct or *AA* stacking than in *AB*-stacked parts. Consequently, edge states arising from *AB*-stacked regions are closer to the Fermi energy than those stemming from *AA* zones. Such nontrivial interplay of edge states and moiré patterns has been evidenced in the identification of bead-like states of moiré edges in graphite with stacking disorder [10]. Hence, it is compelling to explore how such localization might be affected by defects [14–17], especially vacancies [18–20], which are themselves the source of localized states. The above-mentioned inhomogeneous interlayer hopping in moiré patterns is, moreover, related to the breaking of electron hole-symmetry at low energies [21,22]. Additionally, issues such as the enhancement of strong correlations near the magic angle in one-dimensional moiré systems [23,24], the nontrivial band topology of twisted bilayer graphene [25], the possible existence of gapped edge states related to its higher-order topology [26], or even corner states [27] in this material, have spurred the experimental exploration of quasi-one-dimensional moiré structures [28–30]. In fact, twisted bilayer graphene nanoribbon (GNR) junctions have been experimentally shown to present highly tunable edge states with energy and spin degeneracy crucially dependent on the edge stacking offset [30]. Despite the progress on fabrication techniques, some defects or impurities might be present either due to the edge-shaping process or to the adsorption of hydrogen in the GNR, so it is relevant to address the role of defects in these twisted moiré QPCs to assess the change induced in their transport properties.

In this work, we study electron transport in QPCs based on TBG in the ballistic regime. In particular, we focus on the impact of single vacancies that can appear during growth

*Corresponding author: pmoles@ucm.es

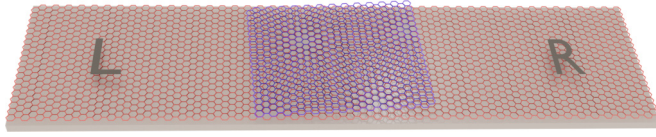


FIG. 1. Sketch of the device that consists of a small graphene flake placed on top of a very long armchair GNR of the same width. The top flake is rotated with respect to the bottom GNR. The two regions of the long GNR away from the top flake are regarded as ideal leads, labeled L (left) and R (right).

and its effect on the transport properties of such QPCs. We analyze the interplay of vacancy-related localized states with edge states, which have been shown to be affected by the inhomogeneous coupling arising from the twist angle. In pristine samples, conductance is quantized for moderately large twist angle (larger than $\simeq 10^\circ$), but quantized plateaus are hardly noticeable on approaching the magic angle ($\simeq 1.1^\circ$). As it is well known, the occurrence of moiré patterns breaks the electron-hole symmetry. However, we find that the electron-hole symmetry is partially restored on increasing the concentration of vacancies. We also explore the consequences of the spatial distribution of vacancies over the QPC, verifying that they have a larger impact when they are mainly located at the central part for systems with armchair edges.

The paper is organized as follows. In Sec. II we present the system and model Hamiltonian used for obtaining electronic transport properties. In Sec. III we present our results in two steps. First, in Sec. III A we investigate pristine QPCs and investigate the dependence of the conductance on the twist angle. Second, in Sec. III B we study the effect of a random distribution of single vacancies on the conductance. Section IV concludes with a brief summary of the results.

II. SYSTEM AND MODEL HAMILTONIAN

The system under consideration consists of a very long armchair GNR, on top of which a ultrasmall graphene flake of the same width is placed. The top flake is rotated with respect to the bottom GNR and it can be viewed as a graphene quantum dot. At 0° rotation angle the flake has an armchair edge aligned with that of the bottom GNR, presenting two zigzag edges at the leads-conductor coupling areas. For nonzero rotation angle, we preserve the armchair edges in the current direction, and chiral edges [31], with mixed zigzag-armchair character, arise in the direction perpendicular to the current. The two regions of the bottom GNR away from the top flake are regarded as ideal leads, denoted left (L) and right (R) in Fig. 1. Therefore, electrons coming from the left lead are scattered off from the middle region that is coupled to the top flake and then they are reflected or transmitted to the right lead. In this way a QPC is created.

The tight-binding Hamiltonian reads as $H_1 + H_2 + H_{\text{inter}}$, where H_ℓ describes the electron dynamics in the lower ($\ell = 1$) and upper ($\ell = 2$) graphene monolayers (the ribbon and the flake, respectively). Since our focus are the low-energy transport properties of the twisted QPC, we use a nearest-neighbor approximation for the intralayer Hamiltonian and include a larger-range interlayer hoppings for the interlayer coupling.

This approach has been successfully employed in twisted bilayer systems [11,32,33] and also in Bernal graphene bilayers [22,34]. The intralayer nearest-neighbor hopping describes the linear dispersion near the Fermi point and the interlayer hoppings provide a low-energy modification of this dispersion with an exponentially decaying coupling within the Slater-Koster approach [22,33]. Hence

$$\mathcal{H}_\ell = - \sum_{\langle i,j \rangle} \gamma_0 c_{\ell i}^\dagger c_{\ell j} + \text{H.c.}, \quad (1a)$$

$$\mathcal{H}_{\text{inter}} = - \sum_{i,j} \gamma_1 e^{-\beta(r_{ij}-d)} c_{1i}^\dagger c_{2j} + \text{H.c.}, \quad (1b)$$

where H.c. stands for Hermitian conjugate and the summation in $\langle i, j \rangle$ runs over nearest-neighbor C atoms. The origin of energy is set at the energy of the C orbital. Here $c_{\ell i}^\dagger$ and $c_{\ell i}$ are the creation and annihilation fermion operators at site i of the monolayer ℓ . The parameters $\gamma_0 = 3.16$ eV and $\gamma_1 = 0.39$ eV, are the intra and interlayer nearest-neighbor hoppings, respectively; $r_{ij} = |\mathbf{r}_i - \mathbf{r}_j|$ is the distance between atoms with positions \mathbf{r}_i and \mathbf{r}_j , each one located on a different layer; $d = 3.35$ Å is the interlayer distance and $\beta = 3$ Å⁻¹ [10]. The summation in (1b) runs over all atom pairs i and j of different layers and it is restricted to $r_{ij} < 6a_0$, with $a_0 = 1.42$ Å being the C-C distance. This parametrization has been proved to provide excellent agreement with *ab initio* calculations of the bands near the Fermi energy of TBG systems [23,24,33,35].

Electron states of the QPC are characterized by the local density of states (LDOS), defined as

$$\rho(\mathbf{r}_i, E) = \sum_\nu |\psi_\nu(\mathbf{r}_i)|^2 \delta(E - E_\nu), \quad (2a)$$

where the summation runs over all eigenstates of the QPC with energy E_ν and $\psi_\nu(\mathbf{r}_i)$ denotes the amplitude at position \mathbf{r}_i of the corresponding eigenstate. The wave function is assumed to be normalized hereafter. Similarly, the density of states (DOS) is calculated from the LDOS as $\rho(E) = \sum_{i=1}^N \rho(\mathbf{r}_i, E)$, where N is the number of atomic positions in the QPC.

The spatial extent of an arbitrary eigenstate ν can also be estimated from the participation ratio (PR)

$$\text{PR}_\nu = \left(\sum_{i=1}^N |\psi_\nu(\mathbf{r}_i)|^4 \right)^{-1}. \quad (2b)$$

Recall that $\text{PR}_\nu \sim 1$ when the eigenstate is localized at a single atom and $\text{PR}_\nu \sim N$ when the eigenstate is extended over the entire QPC. Finally, electron transport properties at low temperature were calculated within the framework of the Landauer-Büttiker formalism [36]. In this formalism, the conductance is calculated in the linear regime (i.e., at low bias) as

$$G(E) = \frac{e^2}{h} \tau(E), \quad (2c)$$

where $\tau(E)$ is the transmission coefficient at energy E . Electrons scatter off the QPC and conductance is found to be dependent on the number of modes which can travel along the device. Calculation of the three magnitudes (2) was performed with the help of the Kwant toolkit [37].

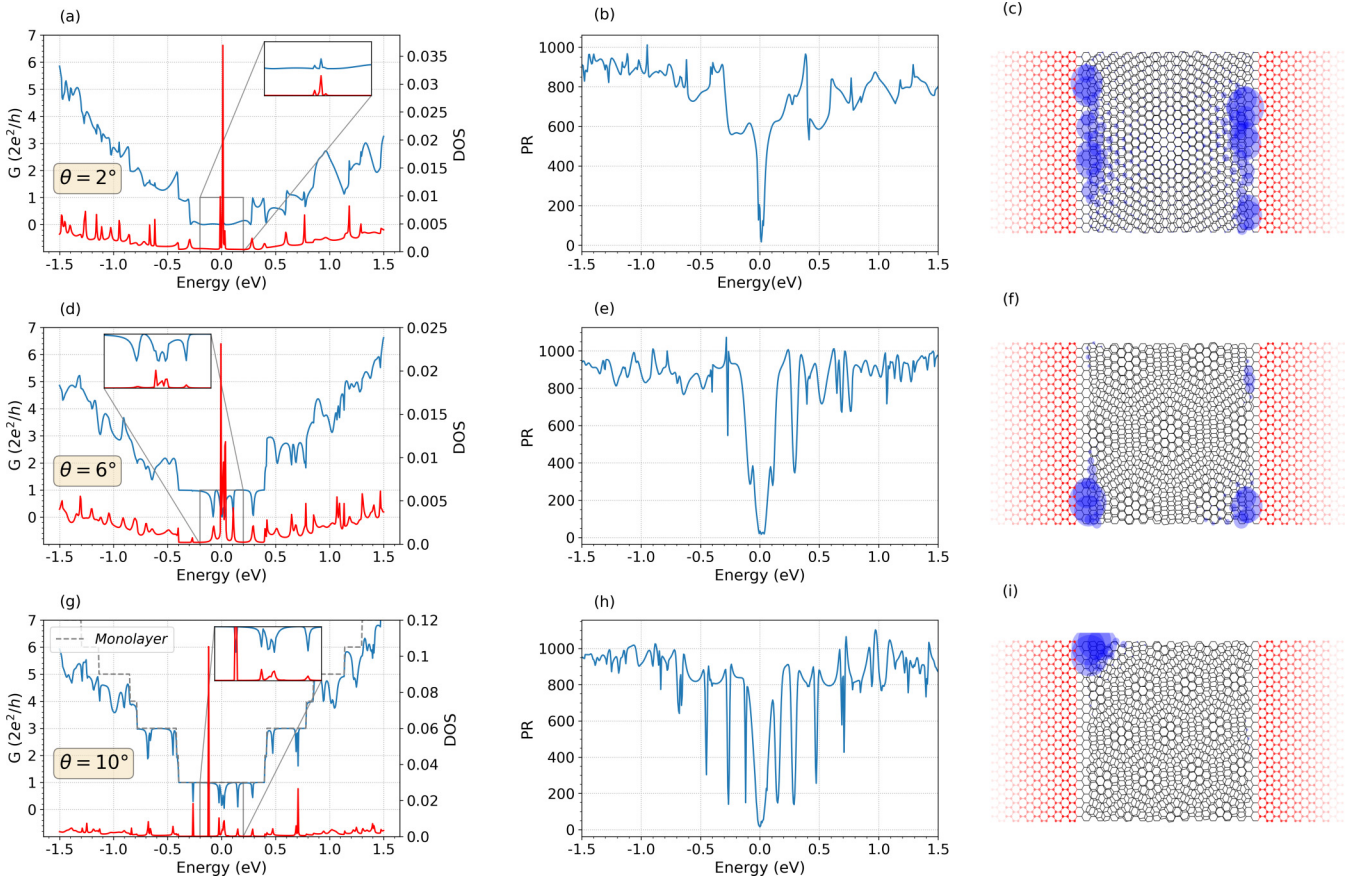


FIG. 2. Leftmost panels show the conductance (blue line) and DOS of the QPC (red line) for rotation angles of (a) $\theta = 2^\circ$, (d) $\theta = 6^\circ$, and (g) $\theta = 10^\circ$. Insets of leftmost panels show an enlarged view of the conductance and DOS. Middle panels show the PR for (b) $\theta = 2^\circ$, (e) $\theta = 6^\circ$, and (h) $\theta = 10^\circ$. The rightmost panels represent the LDOS at energy $E = 0$ eV for each rotation angle. The radii of the circles are proportional to the LDOS on each atom. Left and right leads appear in red color.

III. RESULTS

Our results were obtained for a QPC of dimensions $5 \times 5 \text{ nm}^2$, which contains of the order of 1900 atoms. This size suffices to observe the moiré pattern at moderately small angles and does not demand excessive computational cost. Due to the electron-hole symmetry breaking, we consider both positive and negative energies in the range ± 1.5 eV around the charge neutrality point.

A. Pristine QPC

First we consider a pristine QPC to assess the electron dynamics in the absence of vacancies. Figure 2 depicts the conductance, PR and LDOS as functions of the energy for rotation angles θ of 2° , 6° , and 10° . The conductance curves are asymmetrical around the charge neutrality point, presenting higher values at negative energies for $\theta = 2^\circ$, but at positive energies in the case of $\theta = 6^\circ$ and $\theta = 10^\circ$. This electron-hole broken symmetry is related to the extent of the interlayer coupling that reaches all neighboring atoms within a circle of 8.52 \AA radius. As discussed in the context of TBG, the coupling between atoms of the same sublattice causes electron-hole symmetry breaking. Furthermore, the conductance presents a marked dependence with the rotation angle.

At $\theta = 10^\circ$ the three plateaus of the quantized conductance are perfectly observable up to ± 0.8 eV and coincide with those of a single GNR. On decreasing the angle the moiré periodicity is less apparent since the flake size becomes smaller than the moiré period and the plateaus of the conductance are smeared out, being barely noticeable for $\theta = 2^\circ$. Figure S1 in the Supplemental Material [38] supports this assertion with more rotation angles, where the nontwisted case $\theta = 0^\circ$ has been also displayed.

If we turn the attention to the DOS, plotted in red in Figs. 2(a), 2(d), and 2(g), it provides information of the continuum of states of the leads as well as the discrete states of the QPC. The DOS presents sharp peaks due to the occurrence of discrete levels that result from quantum confinement effects in the upper finite flake of the QPC, which can be viewed as a coupled quantum dot to a GNR conductor. These states are confined at the top flake and interfere with the continuum states of the GNR as well-known Fano-type antiresonances. This gives rise to sharp dips in the conductance curves (especially distinguished at the plateaus), which are also identified by the coincidence in energy with the DOS peaks due to the discrete states. This behavior was also observed in bilayer flakes with *AA* or *AB* stacking for which these destructive interferences were also analyzed [39,40].

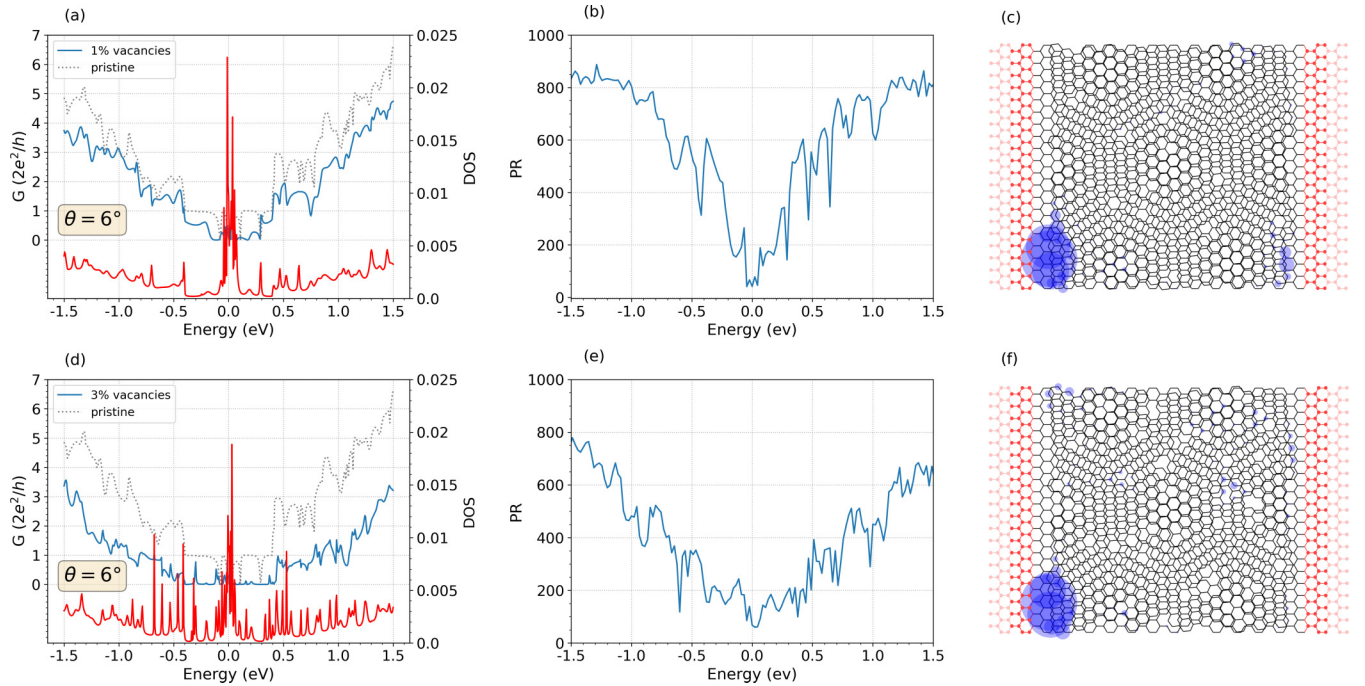


FIG. 3. Leftmost panels show conductance of a pristine QPC (gray dashed line) and a defective QPC (blue line) at $\theta = 6^\circ$. In the later case, vacancies are randomly distributed over the whole QPC with concentration (a) 1% and (d) 3%. The DOS of the QPC is also displayed (red line). Middle panels show the PR corresponding to panels (a) and (d), respectively. The rightmost panels show the LDOS at $E = 0$ eV for each concentration. The radii of the circles are proportional to the LDOS on each atom.

Among the confined states mentioned before, those at $E = 0$ eV are remarkable since they exhibit a huge peak in the DOS for all rotation angles in Fig. 2. The states associated to these peaks are highly localized, in accordance with the small value of the PR observed in Fig. 2. The insets of the left panels of Fig. 2 show an enlarged view of the conductance and DOS close to the charge neutrality point. It is found that there are two very close peaks at positive and negative energy. The spatial extent of the corresponding states can be revealed by the atom-resolved LDOS, presented in the rightmost panels of Fig. 2. It indicates the edge-like character of the states, localized at the transverse edge of the upper flake of the QPC, perpendicularly to the direction of the current. In the case of $\theta = 2^\circ$, the states spread along the edge, while in the other two angles they are corner-like states. This can be explained in view of the zigzag character of the edge that is well known to cause the appearance of zero energy states in graphene. The transverse edge is mainly zigzag for $\theta = 2^\circ$, but on increasing the angle, the edges become more chiral (i.e., a larger mixture of zigzag and armchair portions [31]) and prevent the spreading of the states. Also, it is worth mentioning that the two edge states for $\theta = 2^\circ$ decay inside the QPC [Fig. 2(c)], but are weakly coupled due to the small size of the QPC. This coupling is responsible for the small shift from the charge neutrality point of the two peaks, which hybridize to form bonding and antibonding states. More localized states and their spatial extent can be found in Fig. S2 of the Supplemental Material [38] for other twist angles. At $|E| > 0.4$ eV the DOS gradually grows as the number of occupied modes of the leads increases.

B. QPC with vacancies

We now turn our attention to the effects of point vacancies located in the QPC on electron transport properties. These defects are introduced by removing atomic sites and the corresponding bonds in both monolayers of graphene. First, we study a random distribution of vacancies over the entire QPC (vacancies are not included in the leads). Next, we restrict the location of the vacancies to the edges and to the middle region of the QPC to elucidate their impact on the conductance.

Transport properties in a nanometric system are found to depend noticeably on the particular arrangement of vacancies of each disorder realization. Hence, an average over different disorder realizations does not provide useful information, as it is usual for nanoscopic systems. Instead, we choose some particular configurations to present the typical electrical response of the QPC. Taking the intermediate angle $\theta = 6^\circ$ of the pristine QPC (Fig. 2) as an example of the twisted angle, we show in Fig. 3 the effect of adding a distribution of vacancies covering at random the entire area of the QPC, for concentrations of 1% and 3% relative to the total QPC sites. The 3% case was generated from the configuration with 1% and adding extra vacancies, so that both concentrations share part of the vacancy positions. A first result observed in Figs. 3(a) and 3(d) is the drop of the conductance and the suppression of the previously smeared out plateaus (with decreasing twist angle) due to scattering. This effect raises with the vacancy concentration. It is also a noticeable gap in the conductance that appears at low energies, which broadens on increasing the concentration. Vacancies in graphene are known to induce localized states with energies close to the Dirac point [41,42].

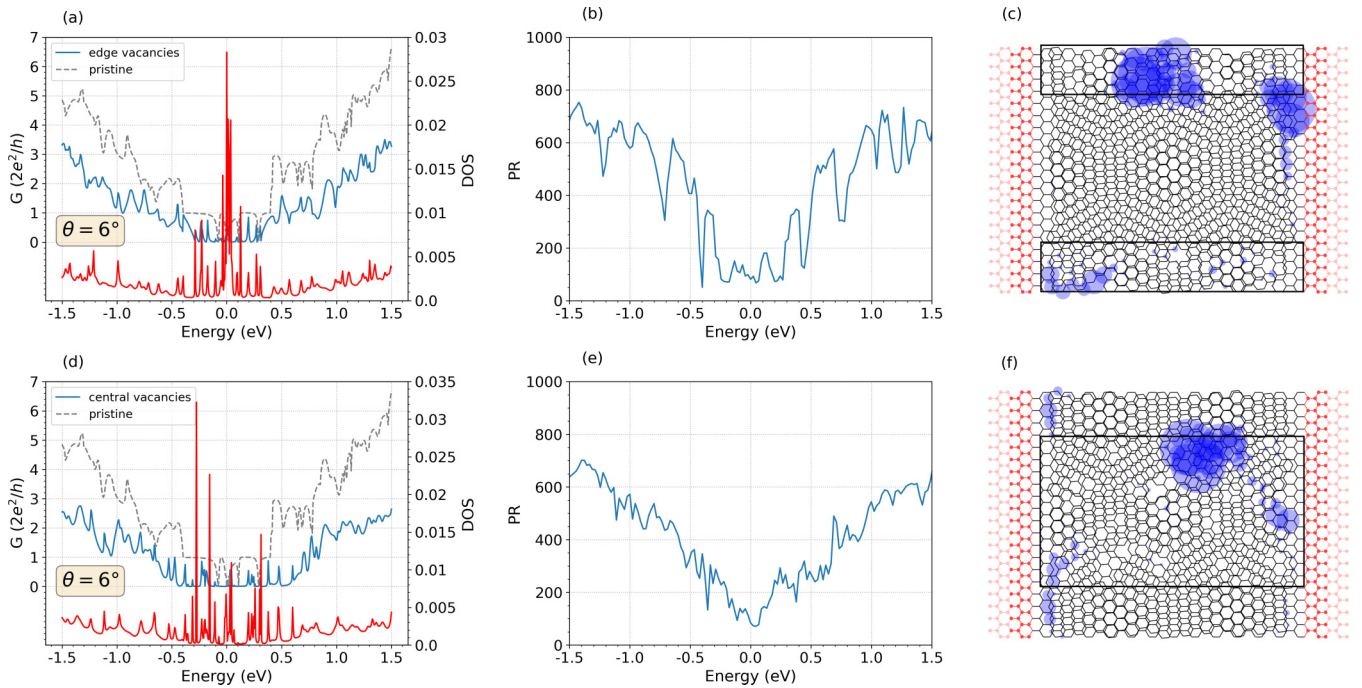


FIG. 4. Conductance as a function of energy of a pristine QPC (gray dashed line) and a defective QPC in the case of $\theta = 6^\circ$ when the vacancies are located at (a) edges and (d) central part of the QPC. Panels (b) and (e) show the PR corresponding to panels (a) and (d), respectively. Panels (c) and (f) display the LDOS at energy $E = 0$ eV for each case. The radii of the circles are proportional to the LDOS on each atom. The concentration of vacancies is 3% in both cases.

These localized states interfere with the continuum of states as Fano resonances, causing zero-conductance dips. These dips were later extensively studied in graphene nanoribbons [43–45], where the shape and energy of the dip depended on the geometry of the edge and the position of the vacancy. However, when the edge is armchair the dip remains around $E = 0$ for both monolayer and bilayer ribbons. In the case of this work, where there are many vacancies, the single vacancy antiresonances add up, leading to the formation of a transport gap around zero energy [45]. The DOS confirms this affirmation, with many peaks flocking together around this energy due to the appearance of vacancy states, as expected [41,43], in contrast to the pristine case presented in Fig. 2.

However, the most intriguing effect caused by vacancies is that the conductance curves become more symmetrical than in the pristine case, and this symmetry turns out to increase with the vacancy concentration [see Figs. 3(a) and 3(d)]. This phenomenon not only occurs for the chosen arrangement of vacancies, but in many other studied configurations, as shown in Fig. S3 in the Supplemental Material [38]. Therefore, we find a recovery of the electron-hole symmetry, clearly broken in twisted bilayer graphene, with the inclusion of vacancies. Broken symmetry for this model of TBG occurs due to the large span of the interlayer hopping which, unlike the usual nearest-neighbor hopping models in monolayer graphene (with hoppings only between different sublattices, A - B), includes also tunnel processes between atoms of the same sublattices, i.e., A - A or B - B . This hopping between atoms of the same sublattice causes electron-hole symmetry breaking [22]. We claim that the addition of vacancies weakens the same-sublattice hopping because it reduces the total number of interlayer tunnel processes. This implies that there

are fewer hoppings between the same sublattices so that the electron-hole symmetry is partially restored.

The PR of electron states is also affected by vacancies. Compared to the pristine case [see Fig. 2(e)], the region with low PR around the charge neutrality point of energy becomes broader on adding vacancies, as it can be observed in Figs. 3(b) and 3(e). This means that states are more localized in this case, according with the previous analysis. Finally, we explore the energy $E = 0$ and plot the LDOS in Figs. 3(c) and 3(f). The localization of the $E = 0$ state around the vacancies can be noticed under a close inspection. However, localization is stronger at the zigzag edges of the top flake; in fact, the $E = 0$ state is mainly located at the edges of the QPC as in the pristine QPC [see Fig. 2(f)].

In addition, we study the dependence of transport properties with the relative position of vacancies inside the QPC in a similar way to Ref. [46]. For that purpose, we study two different spatial configurations of vacancies located at the edge and central regions. In the first configuration, we add vacancies randomly but restricted inside two areas at the longitudinal edges of the QPC, i.e., those parallel to the current direction. Each area covers $1 \times 5 \text{ nm}^2$ [see the areas in Fig. 4(c)]. In the second configuration, we restrict the random vacancies only to the middle region of the QPC, in an area of $3 \times 5 \text{ nm}^2$ [see the area in Fig. 4(f)]. The sum of the areas with possible vacancies of the first and second configurations gives the entire flake area. The vacancy concentration is the same for both configurations, namely, 3% relative to the total QPC sites. It is observed that, for the edge geometry studied in this work, with armchair edges in the direction of the current, vacancies located at the edges are less detrimental for electron transport, producing a smaller drop in the conductance than

the vacancies placed in the middle region [Figs. 4(a) and 4(d)]. This can be explained by analyzing the spatial distribution of the electronic wave function in the flake. The amplitude of the wave function of an armchair system practically vanishes at the edges, which causes the overlap with localized vacancy states to be smaller when vacancies are located at the edges. Therefore, the detrimental effect on the conductance is less compared to the case of vacancies localized at the central part of the flake. This also explains the smaller conduction gap at the edge configuration. In both configurations the number of vacancies is equal to the case of the distribution spread over the entire QPC of Fig. 3(f). However, as the defects are restricted to smaller regions in the configuration with vacancies at the edges, the intervacancy distance is lower. The vacancies being closer, their local densities add up, yielding a larger LDOS in Figs. 4(c) and 4(f). Notice that, in this case, the LDOS is not dominated by localization at the edges, as it was the situation depicted in Fig. 3(f).

IV. CONCLUSION

In summary, we studied numerically electron transport through QPCs made of twisted bilayer GNRs at low temperature in the linear regime. The twist angle determines the electronic conductance of pristine samples. On one side, decreasing the angle to approach the magic angle ($\theta \sim 1.1^\circ$)

makes the quantized plateaus hardly observable. On the other side, the occurrence of moiré patterns break the electron-hole symmetry, as revealed by the conductance curves when the Fermi level is shifted from the charge neutrality point. We also considered fabrication imperfections in the form of single vacancies randomly distributed over the QPC. We studied three different arrangements of the vacancies, namely, uniformly spread over the entire QPC, located in the central region of the QPC or at the edges of the QPC. Remarkably, the electron-hole symmetry is partially recovered upon increasing the concentration of vacancies that are uniformly distributed over the QPC. The recovery can be attributed to the reduction of the effective interlayer coupling. Finally, the relevance of edge states in the electron transport is determined from the smaller detrimental effect of the conductance when the vacancies are located at the edges.

ACKNOWLEDGMENTS

This work was supported by the Spanish Ministry of Science and Innovation (Grants No. PID2019-106820RB-C21 and No. PID2022-136285NB-C31). We also acknowledge the support from the “(MAD2D-CM)-UCM” project funded by Comunidad de Madrid; by the Recovery, Transformation, and Resilience Plan; and by NextGenerationEU from the European Union.

-
- [1] K. Sakanashi, N. Wada, K. Murase, K. Oto, G.-H. Kim, K. Watanabe, T. Taniguchi, J. P. Bird, D. K. Ferry, and N. Aoki, *Appl. Phys. Lett.* **118**, 263102 (2021).
 - [2] W. Han, R. K. Kawakami, M. Gmitra, and J. Fabian, *Nat. Nanotechnol.* **9**, 794 (2014).
 - [3] J. Li, K. Wang, K. J. McFaul, Z. Zern, Y. Ren, K. Watanabe, T. Taniguchi, Z. Qiao, and J. Zhu, *Nat. Nanotechnol.* **11**, 1060 (2016).
 - [4] N. Tombros, A. Veligura, J. Junesch, M. H. D. Guimarães, I. J. Vera-Marun, H. T. Jonkman, and B. J. van Wees, *Nat. Phys.* **7**, 697 (2011).
 - [5] M. T. Allen, J. Martin, and A. Yacoby, *Nat. Commun.* **3**, 934 (2012).
 - [6] H. Overweg, H. Eggimann, X. Chen, S. Slizovskiy, M. Eich, R. Pisoni, Y. Lee, P. Rickhaus, K. Watanabe, T. Taniguchi, V. Fal’ko, T. Ihn, and K. Ensslin, *Nano Lett.* **18**, 553 (2018).
 - [7] H. Overweg, A. Knothe, T. Fabian, L. Linhart, P. Rickhaus, L. Wernli, K. Watanabe, T. Taniguchi, D. Sánchez, J. Burgdörfer, F. Libisch, V. I. Fal’ko, K. Ensslin, and T. Ihn, *Phys. Rev. Lett.* **121**, 257702 (2018).
 - [8] J. M. Caridad, S. R. Power, M. R. Lotz, A. A. Shylau, J. D. Thomsen, L. Gammelgaard, T. J. Booth, A.-P. Jauho, and P. Bøggild, *Nat. Commun.* **9**, 659 (2018).
 - [9] V. Clericò, J. A. Delgado-Notario, M. Saiz-Bretín, C. H. Fuentevilla, A. V. Malyshev, J. D. Lejarreta, E. Diez, and F. Domínguez-Adame, *Physica Status Solidi (a)* **215**, 1701065 (2018).
 - [10] E. S. Morell, R. Vergara, M. Pacheco, L. Brey, and L. Chico, *Phys. Rev. B* **89**, 205405 (2014).
 - [11] E. S. Morell, P. Vargas, P. Häberle, S. A. Hevia, and L. Chico, *Phys. Rev. B* **91**, 035441 (2015).
 - [12] M. Pelc, E. S. Morell, L. Brey, and L. Chico, *J. Phys. Chem. C* **119**, 10076 (2015).
 - [13] D. A. Bahamon, G. Gómez-Santos, and T. Stauber, *Nanoscale* **12**, 15383 (2020).
 - [14] P. Lucignano, D. Alfè, V. Cataudella, D. Ninno, and G. Cantele, *Phys. Rev. B* **99**, 195419 (2019).
 - [15] E. H. Hwang and S. Das Sarma, *Phys. Rev. Res.* **2**, 013342 (2020).
 - [16] J. H. Wilson, Y. Fu, S. Das Sarma, and J. H. Pixley, *Phys. Rev. Res.* **2**, 023325 (2020).
 - [17] Y. Skrypnik and V. Loktev, *Low Temp. Phys.* **45**, 1310 (2019).
 - [18] K. Ulman and S. Narasimhan, *Phys. Rev. B* **89**, 245429 (2014).
 - [19] A. S. Minkin, I. V. Lebedeva, A. M. Popov, and A. A. Knizhnik, *Phys. Rev. B* **104**, 075444 (2021).
 - [20] M. Anđelković, L. Covaci, and F. M. Peeters, *Phys. Rev. Mater.* **2**, 034004 (2018).
 - [21] Y. Cao, V. Fatemi, S. Fang, K. Watanabe, T. Taniguchi, E. Kaxiras, and P. Jarillo-Herrero, *Nature (London)* **556**, 43 (2018).
 - [22] E. McCann and M. Koshino, *Rep. Prog. Phys.* **76**, 056503 (2013).
 - [23] O. Arroyo-Gascón, R. Fernández-Perea, E. S. Morell, C. Cabrillo, and L. Chico, *Nano Lett.* **20**, 7588 (2020).
 - [24] O. Arroyo-Gascón, R. Fernández-Perea, E. S. Morell, C. Cabrillo, and L. Chico, *Carbon* **205**, 394 (2023).
 - [25] M. Koshino, *Phys. Rev. B* **99**, 235406 (2019).
 - [26] M. J. Park, Y. Kim, G. Y. Cho, and S. B. Lee, *Phys. Rev. Lett.* **123**, 216803 (2019).
 - [27] M. J. Park, S. Jeon, S. Lee, H. C. Park, and Y. Kim, *Carbon* **174**, 260 (2021).

- [28] C. Chen, Y. Lin, W. Zhou, M. Gong, Z. He, F. Shi, X. Li, J. Z. Wu, K. T. Lam, J. N. Wang, F. Yang, Q. Zeng, J. Guo, W. Gao, J.-M. Zuo, J. Liu, G. Hong, A. L. Antaris, M.-C. Lin, W. L. Mao *et al.*, *Nat. Electron.* **4**, 653 (2021).
- [29] M. Fortin-Deschênes, R. Pu, Y.-F. Zhou, C. Ma, P. Cheung, K. Watanabe, T. Taniguchi, F. Zhang, X. Du, and F. Xia, *Nano Lett.* **22**, 6186 (2022).
- [30] D. Wang, D.-L. Bao, Q. Zheng, C.-T. Wang, S. Wang, P. Fan, S. Mishra, L. Tao, Y. Xiao, L. Huang, X. Feng, K. Müllen, Y.-Y. Zhang, R. Fasel, P. Ruffieux, S. Du, and H.-J. Gao, *Nat. Commun.* **14**, 1018 (2023).
- [31] W. Jaskólski, A. Ayuela, M. Pelc, H. Santos, and L. Chico, *Phys. Rev. B* **83**, 235424 (2011).
- [32] E. Suárez Morell, M. Pacheco, L. Chico, and L. Brey, *Phys. Rev. B* **87**, 125414 (2013).
- [33] X. Lin and D. Tománek, *Phys. Rev. B* **98**, 081410(R) (2018).
- [34] B. Partoens and F. M. Peeters, *Phys. Rev. B* **74**, 075404 (2006).
- [35] E. S. Morell, J. D. Correa, P. Vargas, M. Pacheco, and Z. Barticevic, *Phys. Rev. B* **82**, 121407(R) (2010).
- [36] S. Datta, *Electronic Transport in Mesoscopic Systems* (Cambridge University Press, Cambridge, England, 1997).
- [37] C. W. Groth, M. Wimmer, A. R. Akhmerov, and X. Waintal, *New J. Phys.* **16**, 063065 (2014).
- [38] See Supplemental Material at <http://link.aps.org/supplemental/10.1103/PhysRevB.109.045415> for further results with more rotation angles and vacancy configurations.
- [39] J. W. González, H. Santos, M. Pacheco, L. Chico, and L. Brey, *Phys. Rev. B* **81**, 195406 (2010).
- [40] J. W. González, H. Santos, E. Prada, L. Brey, and L. Chico, *Phys. Rev. B* **83**, 205402 (2011).
- [41] Y. Ma, P. O. Lehtinen, A. S. Foster, and R. M. Nieminen, *New J. Phys.* **6**, 68 (2004).
- [42] V. M. Pereira, F. Guinea, J. M. B. Lopes dos Santos, N. M. R. Peres, and A. H. Castro Neto, *Phys. Rev. Lett.* **96**, 036801 (2006).
- [43] T. C. Li and S.-P. Lu, *Phys. Rev. B* **77**, 085408 (2008).
- [44] Y.-J. Xiong and X.-L. Kong, *Phys. B: Condens. Matter* **405**, 1690 (2010).
- [45] A. Orlof, J. Ruseckas, and I. V. Zozoulenko, *Phys. Rev. B* **88**, 125409 (2013).
- [46] S. Ihnatsenka and G. Kirczenow, *Phys. Rev. B* **80**, 201407(R) (2009).